Air entrainment dynamics of aqueous polymeric droplets from dilute to semidilute unentangled regimes

Cite as: Phys. Fluids **34**, 113105 (2022); https://doi.org/10.1063/5.0130251

Submitted: 10 October 2022 • Accepted: 01 November 2022 • Accepted Manuscript Online: 03 November 2022 • Published Online: 15 November 2022









ARTICLES YOU MAY BE INTERESTED IN

Dual nature of volatility on drop wetting dynamics of acetone-isopropanol mixtures on ultrathin smooth oil films

Physics of Fluids **35**, 012115 (2023); https://doi.org/10.1063/5.0131299

Drop impact dynamics on solid surfaces

Applied Physics Letters 121, 210501 (2022); https://doi.org/10.1063/5.0124256

Drop impact on a sessile soap bubble

Physics of Fluids 34, 122116 (2022); https://doi.org/10.1063/5.0129427





Air entrainment dynamics of aqueous polymeric droplets from dilute to semidilute unentangled regimes

Cite as: Phys. Fluids 34, 113105 (2022); doi: 10.1063/5.0130251 Submitted: 10 October 2022 · Accepted: 1 November 2022 · Published Online: 15 November 2022







Ziwen He, 🕟 Huy Tran, 🕞 and Min Y. Pack^{a)} 🕞



AFFILIATIONS

Department of Mechanical Engineering, Baylor University, One Bear Place No. 97356, Waco, Texas 76798, USA

a) Author to whom correspondence should be addressed: Min Pack@baylor.edu

ABSTRACT

Recent studies have revealed the air-cushioning effect of droplet impact upon various surfaces and although pure water droplets have extensively been studied, the air entrainment dynamics for aqueous polymeric droplets was the focus of this study. Herein, droplets of low to moderate Weber numbers, We $\sim O(1-10)$, displayed air film thickness gradients which was strongly influenced by the viscoelastic properties of the aqueous polymeric droplets in the dilute to the semidilute unentangled regimes. Aqueous polyethylene oxide droplets impacting a smooth thin oil film surface formed a submicrometer air layer, moments prior to impact, which was tracked by a high-speed total internal reflection microscopy technique. The radial changes in the air film thickness were related to the polymer concentration, thus providing an alternative tool for comparing the rheometer-derived overlap concentrations with a contactless optical technique.

Published under an exclusive license by AIP Publishing, https://doi.org/10.1063/5.0130251

INTRODUCTION

Aqueous polymeric droplet impact dynamics provides a platform for understanding the physics of a plethora of commercial and natural applications, including, but not limited to, spray deposition (i.e., agrochemicals, ^{1,2} painting, ³ cooling, ^{4,5} combustion ⁶), inkjet printing, ^{7,8} and respiratory droplet dispersal. ^{9,10} Nevertheless, studies attempting to discern the role of viscoelasticity in the deposition dynamics of polymeric droplets have proven to be challenging. 11 In the absence of a contact line, such as in the early stages of droplet impact, the underlying air decelerates the droplet significantly, generating the entrapment of air in the form of a central dimple as well as an exceedingly thin air film underneath. While recent work has uncovered the rich physics of Newtonian drops, the role of polymer additives on the air entrainment dynamics remains an underexplored topic. This study thus seeks to understand the role of viscoelasticity in the air entrainment of droplets beyond the dilute regime into the semidilute unentangled regime, yet below entanglement concentrations. 13,1

During the droplet impact process, wetting is initiated as a contact line forms with the removal of the interstitial air layer between the droplet and the substrate. However, the entrained air gap can prevent contact entirely, and the non-contact dynamics is especially pronounced under the commonplace Leidenfrost conditions¹⁵ (i.e., when the droplet impacts a heated surface such that it levitates over a thin vapor film 11). The ability with which the droplet is capable of removing the interstitial air film determines whether the droplet may bounce, deposit, splash, or undergo other complex morphologies. Many studies have probed the air entrainment phenomenon underneath droplet impacts through theoretical modeling, experiments, and simulations. 8,16-49 The role of the droplet viscosity alone has generated unique observations with regard to the spreading air film lifting off of the surface with the slope decreasing with viscosity moments prior to the inception of wetting.²

The droplet impact dynamics with the addition of polymers is unique due to the diversity of the polymer types and the rheological signatures of the polymers at varying concentrations between the dilute and entangled regimes. 13,14,29,51-54 The role of extensional rheology has particularly been elusive in the impact dynamics. For instance, polymer additives in the dilute regime tend to suppress the rebound of droplets, where the increase in the extensional viscosity was initially proposed to be the dominant mechanism by Bergeron et al. 55 and later attributed to energy dissipation near the contact line.^{56,57} With the contact line removed via the Leidenfrost effect, Bertola showed that the added polymers in the dilute regime enhanced the final droplet bouncing height, which was reportedly unrelated to the extensional rheology of the droplets.⁵⁸ However, Pack et al. attributed the delay in the failure of the air film by increasing polymer concentrations in the dilute regime, notably due to extensional effects.²

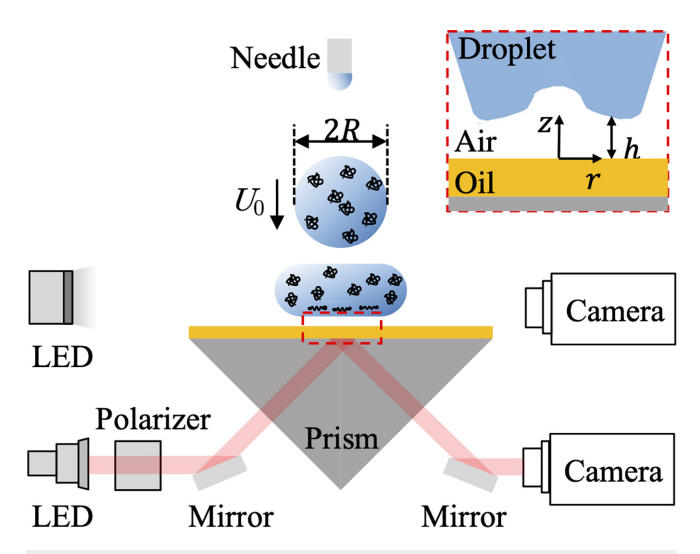


FIG. 1. A schematic of the total internal reflection microscopy (TIRM) experimental technique and the droplet impact setup (not to scale). The dashed box displays the entrained air underneath the impacting droplet as the region of interest.

Beyond the dilute regime, how does the increase in polymer concentration affect the air entrainment dynamics prior to the entanglement concentrations? In this study, we show that the air film is attenuated with the increasing polymer concentration in the semidilute unentangled regime. Utilizing a combination of a high-speed total internal reflection microscopy (TIRM) technique and a rheometer, an alternative means by which the critical overlap concentration, c^* , may be determined is presented.

MATERIALS AND METHODS

Polyethylene oxide (PEO) (Sigma-Aldrich, product no. 189464, $M_{\rm V}\sim 4\,{\rm MDa}$) was chosen as the model polymer with concentrations, c, between $c\approx 5$ and 4000 ppm, produced by a serial dilution. The polymer was initially dispersed in a glass vial via a magnetic stirrer set at 80 rpm in ultrapure de-ionized water (Synergy UV, MilliporeSigma). A pycnometer was used to measure the polymer solution densities, ρ , and showed negligible change across all concentrations ($\rho=0.998-1.001\,{\rm g\,ml^{-1}}$). For the side view of the droplet impact process across all polymer concentrations, the average droplet radius $R=1.11\pm0.04\,{\rm mm}$ was measured at least in triplicates at every release height. A high-speed camera (Phantom V211) at 8000 fps was used to record the side view of droplet impact to measure R and the initial velocity, U_0 .

Thin viscous oil films with an average thickness of $3.2\pm0.6\,\mu\mathrm{m}$ averaged over 20 measurements based on the oil film weight, density, and the glass slide surface area—assuming uniform coating—were used to limit asperity-induced random collapse of the air film, similar to past investigations. ^{21,28,29,37,59,60} To reduce the compliance of the film, ⁵⁹ the viscosity of the silicone oil was kept at 1080 mPa s, while the thickness was minimized.

Due to the importance of the existence of a contact line, observing the droplets from the bottom using the TIRM technique provided direct evidence of the apparent contact of droplets on surfaces as done in the previous studies. 5,24,25,28,29,33,35,36,38 The droplet impact system was enclosed in a custom-built chamber where relative humidity and temperature were tracked. The air film, h, underneath the impacting droplet, was imaged using the TIRM technique (see Fig. 1). A monochromatic 625 nm LED light (ThorLabs M625L4) was p-polarized and was directed to a right-angled prism using a mirror with an angle of 22.5° to the horizontal so that the incident angle of the light beam at the top surface of the prism was $\approx 45^{\circ}$, where total internal reflection occurs at the oil-air interface. Once the approaching droplet entered within the evanescent field, the light was frustrated, allowing for the grayscale intensity changes to be converted to the absolute height changes. A second high-speed camera (Photron NOVA S9) with a frame rate of 25 000 fps connected to a Mitutoyo long working distance $5\times$ objective (3.4 $\mu m/pixel$) was used to capture the TIRM

The rheology of the polymer solution was tracked using a rheometer (Anton Paar MCR 302e) equipped with a cone-plate geometry (a diameter of 59.976 mm and an angle of 0.986°). The temperature was kept at a constant $20.0\pm0.1\,^{\circ}\text{C}$ using the air-cooled Peltier system. Before the rheological measurement, all PEO solutions were presheared with a shear rate of $\dot{\gamma}=10\,\text{s}^{-1}$ for 2 min with a wait time of another 2 min for the samples to relax. A custom-built solvent trap was used to minimize the variation of the solution properties due to evaporation during the measurement.

Table I summarizes the parameters of polymer solutions with various concentrations ranging between c=50 and 4000 ppm. The Deborah number, $De=\tau_e/t_s$, and Capillary number $Ca_d=\eta_0 U_0/\sigma$ show the influence of the extensional relaxation times to the spreading times as well as the viscous to surface forces, respectively. $c^*\approx 461$ ppm is the critical overlap concentration derived from the rheometer utilizing the changes in the specific viscosity of the PEO solutions across all concentrations. A custom pendant droplet method was used to measure the surface tension of the polymer droplets. Although increasing the amount of PEO reduces the surface tension σ (\sim 15.8%) at low

TABLE I. The parameter space of the polymer solutions as a function of concentration.

c (ppm)	50	200	400	500	750	1000	2000	4000
c/c^*	0.11	0.43	0.87	1.08	1.62	2.17	4.34	8.68
η_0 (mPa s)	1.05	1.21	1.8	2.52	2.92	4.47	10.5	43.6
$\sigma (\mathrm{m N m^{-1}})$	67.34 ± 0.7	63.70 ± 0.51	62.46 ± 0.36	63.40 ± 0.12	62.58 ± 0.34	63.33 ± 0.44	63.33 ± 0.43	61.82 ± 0.17
$\tau_{\rm s}$ (ms)	0.51	2.02	2.58	3.75	4.17	4.33	17.71	39.62
$\tau_{\rm e}$ (ms)	1.50	4.64	8.95	9.24	11.46	14.86	25.20	36.93
De	0.56	1.73	3.33	3.43	4.26	5.53	9.38	13.74
$Ca_{\rm d}$	0.01	0.013	0.015	0.02	0.023	0.032	0.075	0.343

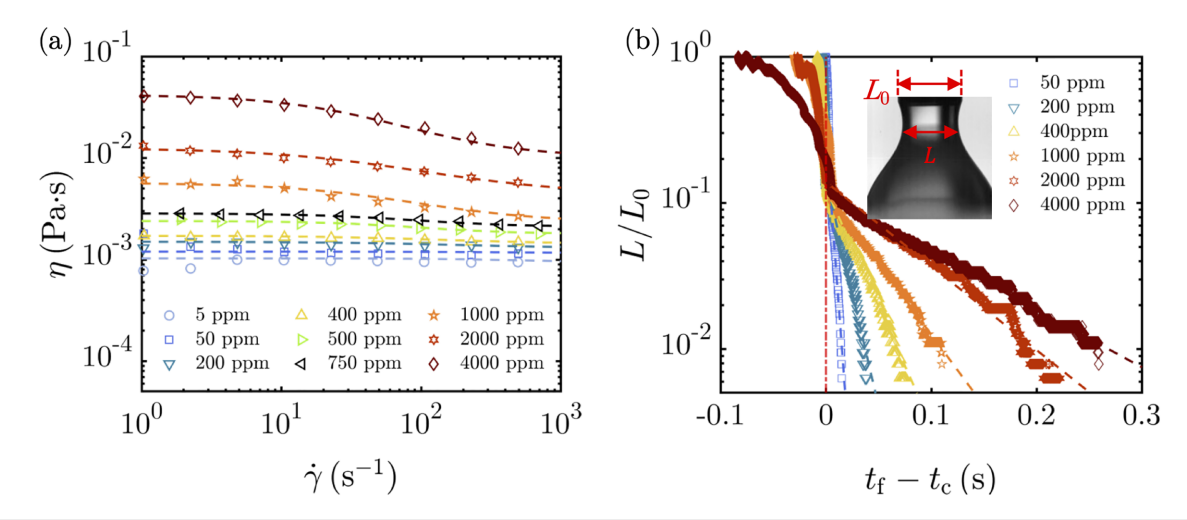


FIG. 2. (a) Shear rheology of aqueous PEO solutions across various concentrations. The dashed lines represent the cross-model fitting [Eq. (1)]. (b) Pinch-off dynamics of the thinning neck using the dripping-onto-substrate method. ⁶² The inset image shows the minimum neck diameter, L_0 , as a function of time for the 400 ppm PEO solution with the needle diameter, L_0 . The time axis was shifted by t_0 so that $t_f - t_0 = 0$ demarcates the transition from the inertia-capillary regime to the elasto-capillary regime. The dashed lines are fittings based on the Entov and Hinch model⁶³ [Eq. (2)] to estimate the uniaxial extensional relaxation time of the polymer solutions.

concentrations, σ becomes independent of the concentration beyond $c=200\,\mathrm{ppm}$.

RESULTS

In Fig. 2, the rheology of the PEO solutions was obtained by applying a shear ramp setting with a shear rate ranging from 1 to $1000 \, \mathrm{s}^{-1}$. The shear viscosity as a function of shear rate exhibited rate-independent behavior for PEO solutions at low concentrations (e.g., $c < 400 \, \mathrm{ppm}$). As the concentration was increased, the shear viscosity showed shear thinning behavior commonly associated with the alignment of polymer chains under shear flow. The rate-dependent shear rheology of the aqueous PEO solutions was well captured by the cross-model fitting, ⁶⁴ with the expression

$$\eta = \frac{\eta_0 - \eta_\infty}{1 + (k\dot{\gamma})^m} + \eta_\infty \,, \tag{1}$$

where η_0 is the zero-shear viscosity, η_∞ is the high-shear rate shear viscosity measured at $1000 \, {\rm s}^{-1}$, $\dot{\gamma}$ is the shear rate, and k and m are fitting parameters for the shear thinning behavior of sample solutions. The zero-shear viscosity calculated from the cross model displayed two orders of magnitude of difference over all of the concentrations as shown in Table I. Using the dripping-onto-substrate-method (DoS), we measured the uniaxial extensional relaxation times of PEO solutions from 50 to 4000 ppm using the following expression developed by Entov and Hinch:

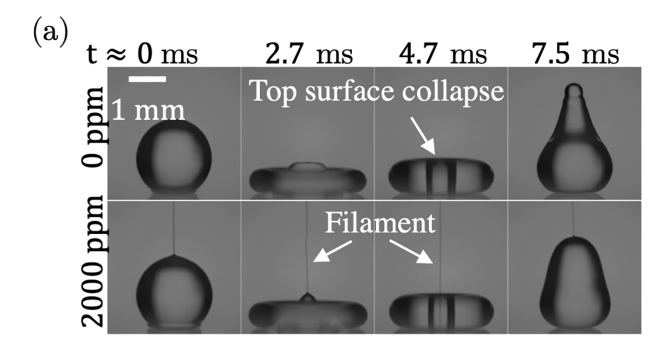
$$\frac{L(t)}{L_0} \approx \left(\frac{G'L_0}{2\sigma}\right)^{\frac{1}{3}} \exp\left(-\frac{t_f - t_c}{3\tau_e}\right),$$
 (2)

where L(t) is the radius of the thinning filament, L_0 is the needle diameter, t_f is the total filament thinning time, t_c is the elasto-capillary transition time, G' is the elastic modulus, σ is the surface tension, and τ_e is the uniaxial extensional relaxation time of the PEO solutions. For Newtonian liquids (e.g., water), the pinch-off process is balanced by the droplet inertia and the capillary force and, thus, denoted as the

inertia-capillary regime. A delay in the pinch-off observed for PEO solutions as displayed by the semi-log plot in Fig. 2(b) is representative of the balance between the elastic and the capillary forces, and thus manifesting the elasto-capillary regime. By performing an exponential fitting on the normalized minimum neck diameter $L(t)/L_0$ within the elasto-capillary regime, as shown in Fig. 2(b) by the decrease in slope with increasing polymer concentration, $\tau_{\rm e}$ is obtained for each concentration which is used as a measure of viscoelasticity of the PEO solutions. We note that although drop impact in our study is biaxial by nature and, thus, the dynamics is more complex, we utilize the uniaxial dynamics as an approximation.

As the impacting droplet approaches the surface, the change in the droplet momentum drives the deformation, where capillary waves propagate along the droplet surface during the spreading phase, as shown in Fig. 3(a) from $t \approx 0$ to 2.7 ms. Figure 3(a) also shows that the spreading dynamics between the water and PEO droplet are remarkably similar at the same Weber number (We = $2 \rho U_0 R/\sigma$). Droplets achieve maximum spreading at a critical time, $t_s \approx 2.7 \, \text{ms}$, with a similar maximum spreading radii. As the capillary waves proceed at $t \approx 4.7$ ms, the top surface of the droplet is inverted and forms a cylindrical air cavity vertically throughout the droplet. Although PEO droplets did not show an appreciable difference from water droplets in terms of the total time for complete liftoff, the morphologies of the lifting droplets were distinguishable as the PEO droplets showed a blunted top surface prior to takeoff. Since the top surface collapse rates are related to the impact velocity U_0 , the velocity was measured by tracking the center of mass of the impacting droplets using the side view images in Fig. 1(a) prior to apparent contact (t < 0 ms). Apparent contact represents the side-view image-derived t = 0 ms, with no regards to actual contact which is more clearly visible in the TIRM setup.

The comparison of U_0 to the release height, H, for water and PEO droplets with $c \approx 50{\text -}4000\,\mathrm{ppm}$ is presented in Fig. 3(b). At higher polymer concentrations [e.g., 2000 ppm in Fig. 3(a)], the droplets formed a thinning filament before pinch-off, which slowed the impact velocity. The release height was increased for higher



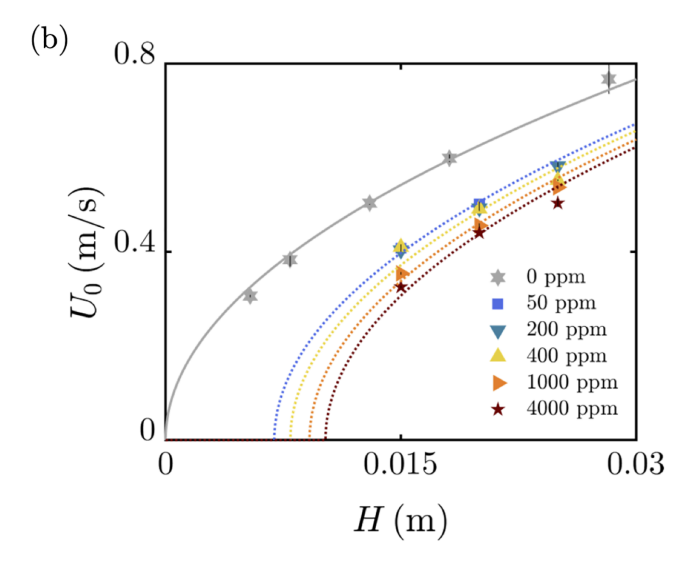


FIG. 3. (a) Side view of droplet impact on the thin oil film. The top row represents water and the bottom row represents a PEO solution of c=2000 ppm at We = 8. The $t\approx 0$ ms was set at the frame when the impacting droplet initially contacts the surface. $t\approx 2.7$ ms was chosen to display the maximum spreading of the droplets. The scale bar represents 1 mm. At high concentrations of PEO solutions (e.g., c=2000 ppm), a thinning filament was observed, which slows down the impact velocity and was accounted for by increasing the droplet release height. (b) The impact velocity, U_0 , was measured against the release height, H, for water and polymer droplets with $c\approx 50$ –4000 ppm. The dotted lines are described by $U_0=\sqrt{2(gH-\Phi)}$.

concentrations to obtain the same impact velocity across the polymer concentrations. The energy balance during the droplet free fall, thus, requires the contributions from kinetic energy, potential energy, surface energy, and viscous dissipation. The surface energy from the formation and stretching of the filament is ignored based on the fact that it is at least an order of magnitude smaller than the other contributions. The impact velocity for the polymeric droplets with a thinning filament may be expressed as $U_0 = \sqrt{2(gH - \Phi)}$, where Φ represents the energy loss per unit mass. Φ was utilized as a fitting parameter to the measurements of U_0 . In the dilute regime, $\Phi = 0.068 - 0.078 \, \mathrm{m}^2 \, \mathrm{s}^{-2}$ with $c \approx 50-400 \, \mathrm{ppm}$, the measured impact velocities were within 5% of each other. In the semidilute unentangled regime, $\Phi = 0.09 - 0.1 \, \mathrm{m}^2 \, \mathrm{s}^{-2}$ with $c \approx 1000-4000 \, \mathrm{ppm}$.

During the impact sequence, the droplet made apparent contact with the substrate, as in Fig. 3(a), but a thin layer of air prevented contact. The non-contact dynamics was captured using the TIRM technique, as depicted schematically in Fig. 1. The air film thickness h was measured radially outward from the center of the air dimple based on the intensity information (e.g., snapshots of the liquid-air interface at $t \approx 0$ and 2.7 ms). For a spreading droplet, the liquid-air interface moved in both the r and z directions over time and squeezed out the air underneath. As the droplet is decelerated by a lubricating air layer, the droplet may sustain enough air underneath to reach maximum spreading. Droplets with higher impact velocities resulted in diminished values of $h_{\rm m}$, which eventually triggered the air film rupture due to intermolecular forces. Figure 4(b) shows the velocity, u_z , of the minimum air film height, $h_{\rm m}$, in the z-direction over the spreading process [see the inset in Fig. 4(b)] with We = $2\rho U_0^2 R/\sigma \approx 8$, where $h_{\rm m}$ decays over time. The air-liquid interface decrement is described by the Reynolds equation given by

$$\frac{\partial h}{\partial t} - \frac{\alpha}{12\eta_{\rm g}r} \frac{\partial}{\partial r} \left(rh^3 \frac{\partial p}{\partial r} \right) + \frac{\partial (hU_{\rm r})}{\partial r} = 0, \tag{3}$$

where α is either 1 or 4 depending on the no slip (i.e., maximum shear stress) or zero-shear stress boundary conditions, respectively. η_g is the air viscosity, p, the driving pressure, and U_r is the rate of spreading of the apparent contact radius. If a vapor source term from evaporation was relevant, the righthand side would need to be adjusted to account for it, which we ignore in this study. The third term on the lefthand side of the equation represents the spreading drop in the film drainage which would counteract the decrease if the effect was strong. However, for the prescribed observation time window, the film drainage only decays and, thus, the drop spreading is ignored. The remaining term to resolve is the pressure gradient, $\frac{\partial p}{\partial x}$, which may be estimated by the initial drop inertia driving the flow given by the dynamic pressure gradient scaling $\frac{\rho_1}{L}\sim \frac{\rho U_0^2}{h},$ resulting in the film drainage scaling to be $h \sim \frac{1}{t}$, which overpredicts the observed thinning rate in Fig. 4. The radial hydrostatic pressure gradient, $\frac{p_g}{L} \sim \frac{\rho g H_d}{L}$, where H_d is the height of the drop and $L \sim \sqrt{hR}$ is an order of magnitude smaller than the capillary pressure gradient, $\frac{p_{\gamma}}{L} \sim \frac{\sigma h}{L^3}$, and thus, we utilize the capillary pressure gradient in Eq. (3)—similar to a bubble impacting a wall⁶⁵—

to obtain the scaling for the air film thickness as $h \sim \left(\frac{\eta_s L^4}{\sigma}\right)^3 t^{-1/3}$, where the prefactor was increased to 1.25×10^{-4} to fit the experimental data in the inset in Fig. 4(b). The scaling is shown to agree well with the data at later times beyond a few frames of the camera > 0.1 ms.

The initial $h_{\rm m}$ at t=0 was set by the initial observation of the dimple, which is sensitive to the camera frame rate and exposure time. By taking the derivative of $h_{\rm m}(t)$ with respect to time, we may quantify the droplet velocity u_z in the z-direction during the spreading process. At t=0, u_z varies from 0.25 to 0.5 mm s⁻¹, which is three orders of magnitude smaller than the impact velocity of 0.5 m s⁻¹, indicating that the impacting droplet has already decelerated before entering the evanescent field. Note that u_z manifests striking similarity across all concentrations during the spreading process, and the variation of u_z across the concentrations is around 28.7% at $t=t_{\rm s}$.

The evolution of the air film topology showed the effects of polymer concentrations on the air entrainment dynamics. The droplet reached maximum spreading at $0 \le t/t_s \le 1$, as shown in Fig. 5.

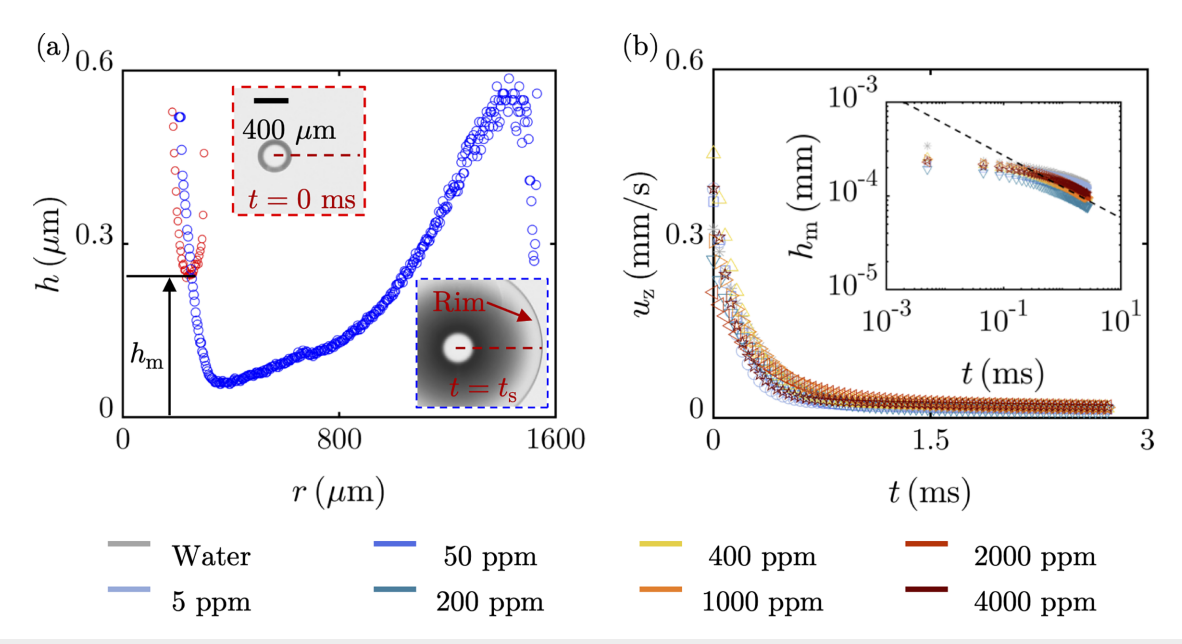


FIG. 4. (a) Snapshots of the bottom view of the liquid–air interface at $t\approx 0$ ms, where the TIRM setup first detects the air dimple, and $t\approx 2.7$ ms, where the droplet reaches maximum spreading ($c\approx 4000$ ppm). The maximum spreading is indicated by the appearance of an outer rim of the bottom view. The air film height, h, is extracted from the intensity distribution along the dashed line. (b) The velocity, u_z , of the minimum air film height, h_m , in the z-direction during the droplet spreading phases across all concentrations. The inset shows h_m as a function of time for $c\approx 5$ –4000 ppm. The black dashed line represents the scaling $h_m \propto t^{-\frac{1}{3}}$ with a prefactor of 1.25 \times 10⁻⁴. All droplets measured above have We ≈ 8 .

During the spreading phase, the topology of the air dimple near r = 0was independent of the concentration and displayed self-similar behavior at the same We, for all time. However, the thicknesses gradient of the air film beyond the air dimple region was altered as a function of c, where it increased with the increasing polymer concentration, from $c \approx 5$ to 500 ppm but decreased between $c \approx 500$ and 4000 ppm [e.g., please see Figs. 5(a)-5(c)]. The retraction stage commenced at $t/t_s = 1$ until $t/t_s \le 3.4$, where the droplet left the field of view. During the retraction phase, the top surface of the droplet carried enough momentum to collapse inward, inverting the top surface. The top surface inversion is caused by the capillary waves along the droplet-air interface, which eventually form a single wave that deforms the top surface enough to be detected in the TIRM setup. Figures 5(d)-5(f) show the strong air dimple inversion induced by the top surface collapse for the 5 ppm case which is yet stunted for the 500 ppm case. Further increasing the concentration to 4000 ppm displayed an incremental change compared with the 500 ppm top surface collapse and yet enhanced the probability of droplets bouncing off of the substrate. Although the onset time of the air dimple inversion is nearly independent of the polymer concentration at the same We, the size of the inversion decreased with the increasing concentration.

The top surface inversion was sometimes large enough to puncture the air film and initiate wetting whereas sometimes the air dimple was significantly deformed but did not break during the retraction. As the concentration was increased, the air film may recover during the retraction stage completely and the rate of recovery increased with concentration. For instance, the air dimple recovered at $t \approx 2.3t_{\rm s}$ for c = 500 ppm PEO droplet, but $t \approx 2t_{\rm s}$ for c = 2000 ppm case [see the inset in Figs. 5(e) and 5(f)]. The total recovery of the dimple was quantified by the time at which the average intensity in the air dimple

region was restored to its original value prior to the top surface collapse.

Figure 6(a) shows the change in specific viscosity, $\eta_{\rm sp}=(\eta_0-\eta_{\rm s})/\eta_{\rm s}$, as a function of the PEO concentrations. The solvent viscosity of the DI water $\eta_{\rm s}\approx 0.95$ mPa s. The critical overlap concentration, c^* , was estimated from the interaction of the dilute and semidilute unentangled regimes where these two regimes may be identified based on the slope transition in Fig. 6(a). $\eta_{\rm sp}\propto c^{0.8}$ in the dilute regime where $c< c^*$, and $\eta_{\rm sp}\propto c^{1.64}$ in the semidilute unentangled regime where $c>c^*$. From the plot, the corresponding specific viscosity $\eta_{\rm sp}\approx 1$ for c^* , indicating the equivalent contribution from the PEO additive and the solvent. 66 In short, the rheometer-derived critical overlap concentration gave rise to $c^*\approx 461$ ppm.

The air film thickness gradients generally follow parabolic curvatures due to the natural shape of the spherical drop before and during maximal spreading, the point at which the drop looks similar to a pancake. Nevertheless, even the central dimple is parabolic and well approximated by a spherical cap as shown previously.⁶⁷ Thus, the curvature of the air film, κ , may be fitted by a quadratic fitting formula of the form, $h = \kappa r^2 + \alpha r + \beta$ to the air film topology at t_s . The vertex of the parabolic fit was set at the point (r_m, h_m) of the minimum air film thickness to where the liquid front displayed the maximal curvature within the upper bound of the optics (e.g., ≈ 600 nm). The curvature was thus obtained for various We and plotted against the polymer concentration, as shown in Fig. 6(b) where the critical overlap concentration occurs at $c^* \approx 500 \, \mathrm{ppm}$ and independent of We. Two distinct regimes between the dilute and the semidilute unentangled regimes were found, which was also observed in Figure 6(a), using the rheometer. While the PEO drops clearly demonstrate the nonmonotonic changes in the air film curvature, Fig. 6(c) shows that for pure glycerol

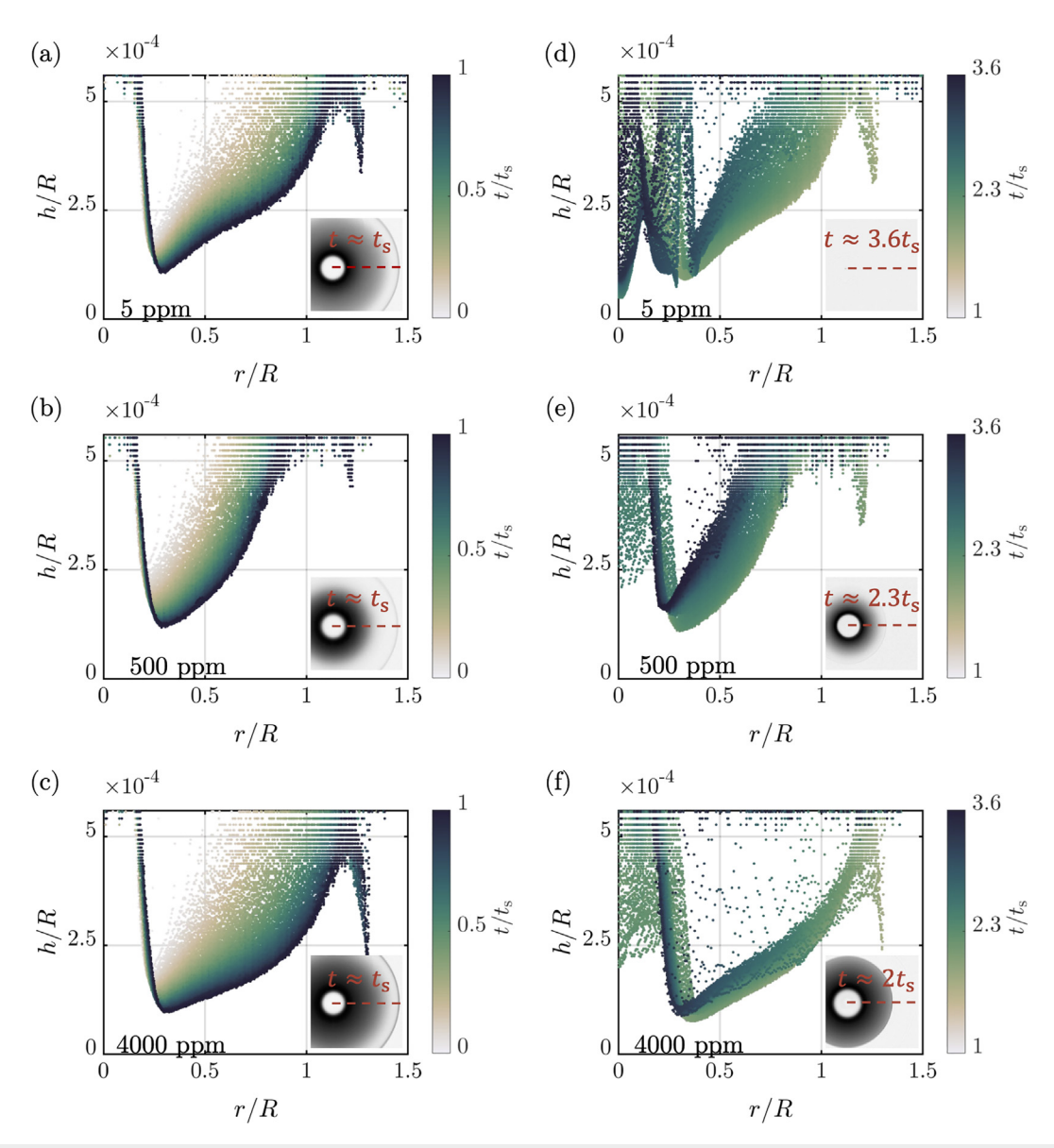


FIG. 5. The normalized spatiotemporal changes in the air film topologies at We \approx 8. (a)–(c) Droplet spreading phase across three concentrations from top to bottom [c=5 (top), 500 (middle), and 4000 ppm (bottom)]. The inset shows the liquid–air interface at the point of maximum spreading, $t/t_{\rm s}=1$. (d)–(f) Droplet retraction stage across the same three polymer concentrations in (a)–(c). The inset was selected at the moment when the air dimple completely recovered from the top surface inversion. The color bar represents the elapsed time normalized by the spreading timescale ($t_{\rm s}\approx 2.67\,{\rm ms}$).

drops in the zero-shear viscosities utilized in this study demonstrate a marked monotonic decrease in the air film curvature with increasing shear viscosity. We, thus, conclude that the air film curvature changes observed in our study are truly due to the rheology of the polymers.

To understand the transition of the air film topology over c^* , we consider two dimensionless numbers De and Ca, which show a similar transition at the critical overlap concentration [please see Fig. 6(d)]. We assume that the relaxation time is a reasonable measure for the polymer solution's extensional behavior, presumably for both uniaxial and biaxial flows. Thus, we may give a tentative description of the transition of

the air film topology over c^* in the following way. In the dilute regime, nearly an order of magnitude increase was observed in De (0.56 \sim 3.33), whereas the increase in Ca_d (0.008 - 0.015) was inappreciable with the increasing concentration. We predict that at lower concentrations, the rise in the extensional viscosity causes the rise in the air film curvature with minimal influence from the shear viscosity during the impulsive deceleration of the droplet in the midst of the droplet spreading phase. However, in the semidilute unentangled regime, the increase in Ca_d (0.02 - 0.343) surpassed the rate of increase in De (3.80 - 13.74), which indicates a strong change in the

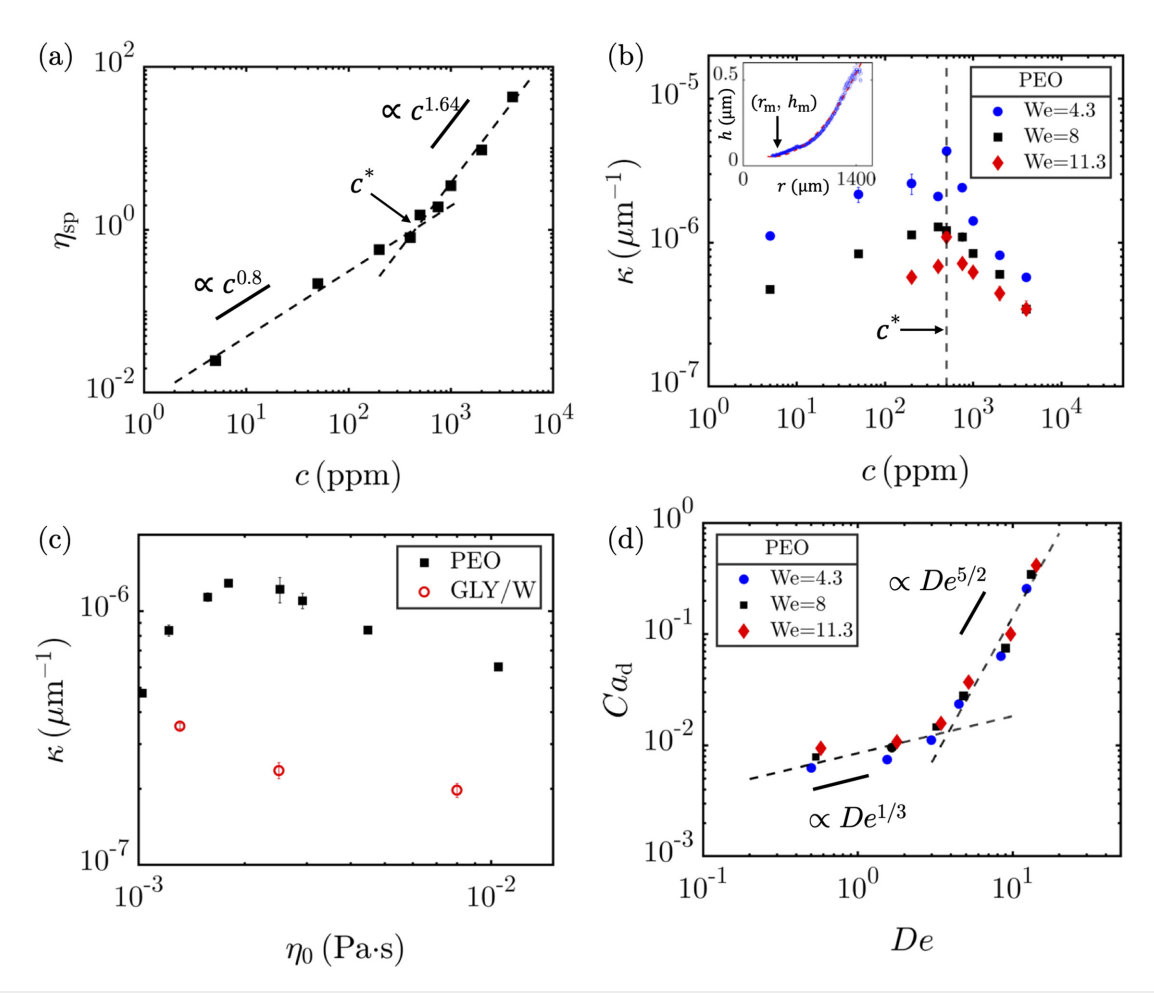


FIG. 6. (a) Specific viscosity as a function of concentration for aqueous PEO solutions reveals two distinctive regimes: dilute regime ($\propto c^{0.8}$) and semidilute unentangled regime ($\propto c^{1.64}$). The rheometer-derived critical overlap concentration was found to be $c^* \approx 461 \,\mathrm{ppm}$. (b) The curvature, κ , of the characteristic air film topology at t_{S} as a function of concentration. The overlap concentration using the TIRM setup was $c^* \approx 500 \,\mathrm{ppm}$. The inset demonstrates the fitting to the characteristic air film topology (blue data points) from the point (r_{m} , h_{m}) of the minimum air film height to the point of maximum curvature distinguishing the air film of interest and the outer rim. (c) The air film curvature for PEO drops and glycerol-water drops (10, 31, and 52.3 wt. %) as a function of the zero-shear viscosity. (d) The capillary number and Deborah number plot across various We.

viscous dissipation within the droplet, albeit to a small value. At sufficiently large concentrations beyond c^* , we expect the overlap of the polymer chains to be able to result in strain softening resulting in the decrease in the extensional viscosity as opposed to the increase observed in the dilute regime. We thus suspect that the strain softening effect will dominate the dynamics, causing the air film curvature to noticeably diminish for concentrations in the semidilute unentangled regime, but more work is needed to find the mechanism underlying the changes in the air film curvatures in future investigations.

CONCLUSIONS

In summary, we demonstrated how the entrained air film profile changed as a function of the droplet polymer concentration beyond the dilute regime into the semidilute unentangled regime for aqueous PEO droplets impacting a smooth non-compliant viscous oil film. When the polymer concentration increased in the dilute regime ($c < c^*$), at fixed We, the thickness gradient of the air film increased. In the semidilute unentangled regime, the polymer concentration increase attenuated the air film thickness gradient. Since the air film thickness gradient reached a maximum near c^* , the future work may show how TIRM may be used as a contactless rheological tool to predict the crossover concentrations across a series of polymer types.

ACKNOWLEDGMENTS

The authors would like to acknowledge Ethan Doupe, Olivia Felton, and Jack Johnson for fruitful discussions. The support for this work was provided by the National Science Foundation under Grant No. PMP-2137341.

AUTHOR DECLARATIONS Conflict of Interest

The authors have no conflicts to disclose.

Author Contributions

Ziwen He: Data curation (equal); Formal analysis (equal); Investigation (equal); Methodology (equal); Visualization (equal); Writing – original draft (equal); Writing – review & editing (equal). Huy Tran: Investigation (equal); Methodology (equal); Software (equal); Visualization (equal). Min Young Pack: Conceptualization (lead); Data curation (supporting); Formal analysis (supporting); Funding acquisition (lead); Investigation (equal); Methodology (equal); Project administration (equal); Resources (equal); Software (equal); Supervision (equal); Validation (equal); Visualization (equal); Writing – original draft (equal); Writing – review & editing (equal).

DATA AVAILABILITY

The data that support the findings of this study are available from the corresponding author upon request.

REFERENCES

- ¹X. Zhao, H. Cui, Y. Wang, C. Sun, B. Cui, and Z. Zeng, "Development strategies and prospects of nano-based smart pesticide formulation," J. Agric. Food Chem. **66**(26), 6504–6512 (2018).
- ²T. Gilet and L. Bourouiba, "Fluid fragmentation shapes rain-induced foliar disease transmission," J. R Soc. Interface 12(104), 20141092 (2015).
- ³F. Nardelli, F. Martini, J. Lee, A. Lluvears-Tenorio, J. La Nasa, C. Duce, B. Ormsby, M. Geppi, and I. Bonaduce, "The stability of paintings and the molecular structure of the oil paint polymeric network," Sci. Rep. 11(1), 14202 (2021).
- ⁴S. V. Ravikumar, J. M. Jha, A. M. Tiara, S. K. Pal, and S. Chakraborty, "Experimental investigation of air-atomized spray with aqueous polymer additive for high heat flux applications," Int. J. Heat Mass Transfer 72, 362–377 (2014).
- ⁵M. Shirota, M. A. J. van Limbeek, C. Sun, A. Prosperetti, and D. Lohse, "Dynamic Leidenfrost effect: relevant time and length scales," Phys. Rev. Lett. 116(6), 064501 (2016).
- ⁶S. Chen and V. Bertola, "Jumps, somersaults, and symmetry breaking in Leidenfrost drops," Phys. Rev. E 94(2), 021102 (2016).
- ⁷E. Tekin, P. J. Smith, and U. S. Schubert, "Inkjet printing as a deposition and patterning tool for polymers and inorganic particles," Soft Matter 4(4), 703–713 (2008).
- ⁸D. Lohse, "Fundamental fluid dynamics challenges in inkjet printing," Annu. Rev. Fluid Mech. **54**(1), 349 (2022).
- ⁹J. Jiang, H. Zhang, W. He, T. Li, H. Li, P. Liu, M. Liu, Z. Wang, Z. Wang, and X. Yao, "Adhesion of microdroplets on water-repellent surfaces toward the prevention of surface fouling and pathogen spreading by respiratory droplets," ACS Appl. Mater. Interfaces 9(7), 6599–6608 (2017).
- ¹⁰Y. Wang, R. Dandekar, N. Bustos, S. Poulain, and L. Bourouiba, "universal rim thickness in unsteady sheet fragmentation," Phys. Rev. Lett. 120(20), 204503 (2018).
- ¹¹V. Bertola, "Effect of polymer concentration on the dynamics of dilute polymer solution drops impacting on heated surfaces in the Leidenfrost regime," Exp. Therm. Fluid Sci. 52, 259–269 (2014).
- ¹²C. Josserand and S. T. Thoroddsen, "Drop impact on a solid surface," Annu. Rev. Fluid Mech. 48(1), 365–391 (2016).
- ¹³ A. Louhichi, C.-A. Charles, S. Arora, L. Bouteiller, D. Vlassopoulos, L. Ramos, and C. Ligoure, "Competition between shear and biaxial extensional viscous dissipation in the expansion dynamics of Newtonian and rheo-thinning liquid sheets," Phys. Fluids 33(7), 073109 (2021).

- ¹⁴A. Louhichi, C.-A. Charles, T. Phou, D. Vlassopoulos, L. Ramos, and C. Ligoure, "Biaxial extensional viscous dissipation in sheets expansion formed by impact of drops of Newtonian and non-Newtonian fluids," Phys. Rev. Fluids 5(5), 053602 (2020).
- 15J. G. Leidenfrost, De Aquae Communis Nonnullis Qualitatibus Tractatus (Ovenius, 1756).
- ¹⁶Strutt, J. W XIII, "Further observations upon liquid jets, in continuation of those recorded in the Royal Society's 'Proceedings' for March and May, 1879," Proc. R. Soc. London 34(220–223), 130–145 (1883).
- ¹⁷W. Bouwhuis, R. C. A. van der Veen, T. Tran, D. L. Keij, K. G. Winkels, I. R. Peters, D. van der Meer, C. Sun, J. H. Snoeijer, and D. Lohse, "Maximal air bubble entrainment at liquid-drop impact," Phys. Rev. Lett. 109(26), 264501 (2012)
- ¹⁸M. V. Chubynsky, K. I. Belousov, D. A. Lockerby, and J. E. Sprittles, "Bouncing off the walls: The influence of gas-kinetic and van der waals effects in drop impact," Phys. Rev. Lett. 124(8), 084501 (2020).
- ¹⁹J. de Ruiter, R. Lagraauw, F. Mugele, and D. van den Ende, "Bouncing on thin air: How squeeze forces in the air film during non-wetting droplet bouncing lead to momentum transfer and dissipation," J. Fluid Mech. 776, 531–567 (2015)
- ²⁰J. de Ruiter, J. M. Oh, D. van den Ende, and F. Mugele, "Dynamics of collapse of air films in drop impact," Phys. Rev. Lett. 108(7), 074505 (2012).
- ²¹C. Hao, J. Li, Y. Liu, X. Zhou, Y. Liu, R. Liu, L. Che, W. Zhou, D. Sun, L. Li, L. Xu, and Z. Wang, "Superhydrophobic-like tunable droplet bouncing on slippery liquid interfaces," Nat. Commun. 6(1), 7986 (2015).
- pery liquid interfaces," Nat. Commun. 6(1), 7986 (2015).

 ²²Z. He, H. Tran, and M. Y. Pack, "Drop bouncing dynamics on ultrathin films," Langmuir 37(33), 10135–10142 (2021).
- ²³E. Klaseboer, R. Manica, and D. Y. C. Chan, "Universal behavior of the initial stage of drop impact," Phys. Rev. Lett. 113(19), 194501 (2014).
- ²⁴J. M. Kolinski, L. Mahadevan, and S. M. Rubinstein, "Lift-off instability during the impact of a drop on a solid surface," Phys. Rev. Lett. 112(13), 134501 (2014).
- 25 J. M. Kolinski, S. M. Rubinstein, S. Mandre, M. P. Brenner, D. A. Weitz, and L. Mahadevan, "Skating on a film of air: Drops impacting on a surface," Phys. Rev. Lett. 108(7), 074503 (2012).
- ²⁶K. Langley, E. Q. Li, and S. T. Thoroddsen, "Impact of ultra-viscous drops: Air-film gliding and extreme wetting," J. Fluid Mech. 813, 647–666 (2017).
- 27J. S. Lee, B. M. Weon, J. H. Je, and K. Fezzaa, "How does an air film evolve into a bubble during drop impact?," Phys. Rev. Lett. 109(20), 204501 (2012).
- ²⁸M. Pack, H. Hu, D. Kim, Z. Zheng, H. A. Stone, and Y. Sun, "Failure mechanisms of air entrainment in drop impact on lubricated surfaces," Soft Matter 13(12), 2402–2409 (2017).
- ²⁹ M. Y. Pack, A. Yang, A. Perazzo, B. Qin, and H. A. Stone, "Role of extensional rheology on droplet bouncing," Phys. Rev. Fluids 4(12), 123603 (2019).
- 30S. T. Thoroddsen, T. G. Etoh, K. Takehara, N. Ootsuka, and Y. Hatsuki, "The air bubble entrapped under a drop impacting on a solid surface," J. Fluid Mech. 545, 203–212 (2005).
- ³¹T. Tran, H. de Maleprade, C. Sun, and D. Lohse, "Air entrainment during impact of droplets on liquid surfaces," J. Fluid Mech. 726, R3 (2013).
- ³²L. Xu, W. W. Zhang, and S. R. Nagel, "Drop splashing on a dry smooth surface," Phys. Rev. Lett. 94(18), 184505 (2005).
- ³³L. Zhang, T. Soori, A. Rokoni, A. Kaminski, and Y. Sun, "Air film contact modes of drop impact on lubricated surfaces under reduced pressures," Phys. Fluids 33(9), 092110 (2021).
- 34G. Liang, Y. Guo, S. Shen, and Y. Yang, "Crown behavior and bubble entrainment during a drop impact on a liquid film," Theor. Comput. Fluid Dyn. 28(2), 159–170 (2014).
- 35J. M. Kolinski, L. Mahadevan, and S. M. Rubinstein, "Drops can bounce from perfectly hydrophilic surfaces," Europhys. Lett. 108(2), 24001 (2014).
- 36P. Chantelot and D. Lohse, "Drop impact on superheated surfaces: Short-time dynamics and transition to contact," J. Fluid Mech. 928, A36 (2021).
- ³⁷H. Y. Lo, Y. Liu, and L. Xu, "Mechanism of contact between a droplet and an atomically smooth substrate," Phys. Rev. X 7(2), 021036 (2017).
- ³⁸L. Chen, J. Wu, Z. Li, and S. Yao, "Evolution of entrapped air under bouncing droplets on viscoelastic surfaces," Colloids Surf., A 384(1), 726–732 (2011).
- ³⁹P. Chantelot and D. Lohse, "Leidenfrost effect as a directed percolation phase transition," Phys. Rev. Lett. 127(12), 124502 (2021).

- ⁴⁰S.-H. Lee, M. Rump, K. Harth, M. Kim, D. Lohse, K. Fezzaa, and J. H. Je, "Downward jetting of a dynamic Leidenfrost drop," Phys. Rev. Fluids 5(7), 074802 (2020).
- ⁴¹D. Roy and S. Basu, "Droplet impact on immiscible liquid pool: Multi-scale dynamics of entrapped air cushion at short timescales," arXiv:2111.13832 (2021)
- ⁴²F. Smith, L. Li, and G. Wu, "Air cushioning with a lubrication/inviscid balance," J. Fluid Mech. 482, 291–318 (2003).
- ⁴³S. Mandre, M. Mani, and M. P. Brenner, "Precursors to splashing of liquid droplets on a solid surface," Phys. Rev. Lett. **102**(13), 134502 (2009).
- ⁴⁴X. Cheng, T.-P. Sun, and L. Gordillo, "Drop impact dynamics: Impact force and stress distributions," Annu. Rev. Fluid Mech. 54(1), 57 (2022).
- 45K. R. Langley, E. Q. Li, I. U. Vakarelski, and S. T. Thoroddsen, "The air entrapment under a drop impacting on a nano-rough surface," Soft Matter 14(37), 7586–7596 (2018)
- ⁴⁶Z. Jian, M. A. Channa, A. Kherbeche, H. Chizari, S. T. Thoroddsen, and M.-J. Thoraval, "To split or not to split: Dynamics of an air disk formed under a drop impacting on a pool," Phys. Rev. Lett. 124(18), 184501 (2020).
- ⁴⁷E. Q. Li, K. R. Langley, Y. S. Tian, P. D. Hicks, and S. T. Thoroddsen, "Double contact during drop impact on a solid under reduced air pressure," Phys. Rev. Lett. 119(21), 214502 (2017).
- ⁴⁸N. I. J. Henman, F. T. Smith, and M. K. Tiwari, "Pre-impact dynamics of a droplet impinging on a deformable surface," Phys. Fluids 33(9), 092119 (2021).
- ⁴⁹L. Rayleigh, "Further observations upon liquid jets, in continuation of those recorded in the Royal Society's 'Proceedings' for March and May, 1879," Proc. R. Soc. London 34, 130–145 (1882), http://www.jstor.org/stable/113978.
- ⁵⁰S. Mishra, S. M. Rubinstein, and C. H. Rycroft, "Computing the viscous effect in early-time drop impact dynamics," arXiv:2108.11497 (2021).
- ⁵¹C.-A. Charles, A. Louhichi, L. Ramos, and C. Ligoure, "Viscoelasticity and elastocapillarity effects in the impact of drops on a repellent surface," Soft Matter 17(23), 5829–5837 (2021).
- ⁵²B. Li, S. Lin, Y. Wang, Q. Yuan, S. W. Joo, and L. Chen, "Promoting rebound of impinging viscoelastic droplets on heated superhydrophobic surfaces," New J. Phys. 22(12), 123001 (2020).

- ⁵³A. A. Mehrizi, S. Lin, L. Sun, Y. Wang, and L. Chen, "Penetration and ligament formation of viscoelastic droplets impacting on the superhydrophobic mesh," Sci. Rep. 12(1), 11920 (2022).
- 54Y. Wang, M. Do-Quang, and G. Amberg, "Impact of viscoelastic droplets," J. Non-Newtonian Fluid Mech. 243, 38–46 (2017).
- 55V. Bergeron, D. Bonn, J. Y. Martin, and L. Vovelle, "Controlling droplet deposition with polymer additives," Nature **405**(6788), 772–775 (2000).
- ⁵⁶D. Bartolo, A. Boudaoud, G. Narcy, and D. Bonn, "Dynamics of non-Newtonian droplets," Phys. Rev. Lett. 99(17), 174502 (2007).
- ⁵⁷M. I. Smith and J. S. Sharp, "Origin of contact line forces during the retraction of dilute polymer solution drops," <u>Langmuir</u> 30(19), 5455–5459 (2014).
- 58V. Bertola, "Dynamic wetting of dilute polymer solutions: The case of impacting droplets." Adv. Colloid Interface Sci. 193–194. 1–11 (2013).
- 59S. Lakshman, W. Tewes, K. Harth, J. H. Snoeijer, and D. Lohse, "Deformation and relaxation of viscous thin films under bouncing drops," J. Fluid Mech. 920, A3 (2021).
- ⁶⁰T. Gilet and J. W. Bush, "Droplets bouncing on a wet, inclined surface," Phys. Fluids 24(12), 122103 (2012).
- ⁶¹K. Ebagninin, A. Benchabane, and B. Karim, "Rheological characterization of poly(ethylene oxide) solutions of different molecular weights," J. Colloid Interface Sci. 336, 360–367 (2009).
- ⁶²J. Dinic, Y. Zhang, L. N. Jimenez, and V. Sharma, "Extensional relaxation times of dilute, aqueous polymer solutions," ACS Macro Lett. 4(7), 804–808 (2015).
- 63V. M. Entov and E. J. Hinch, "Effect of a spectrum of relaxation times on the capillary thinning of a filament of elastic liquid," J. Non-Newtonian Fluid Mech. 72(1), 31–53 (1997).
- ⁶⁴M. M. Cross, "Rheology of non-Newtonian fluids: A new flow equation for pseudoplastic systems," J. Colloid Sci. 20(5), 417–437 (1965).
- ⁶⁵E. Esmaili, P. Shukla, J. D. Eifert, and S. Jung, "Bubble impact on a tilted wall: Removing bacteria using bubbles," Phys. Rev. Fluids 4(4), 043603 (2019).
- ⁶⁶C. D. V. Martínez Narváez, J. Dinic, X. Lu, C. Wang, R. Rock, H. Sun, and V. Sharma, "Rheology and pinching dynamics of associative polysaccharide solutions," <u>Macromolecules</u> 54(13), 6372–6388 (2021).
- ⁶⁷D. Panchanathan, P. Bourrianne, P. Nicollier, A. Chottratanapituk, K. K. Varanasi, and G. H. McKinley, "Levitation of fizzy drops," Sci. Adv. 7(28), eabf0888 (2021).